Progress In Electromagnetics Research, Vol. 142, 463–483, 2013

FULL-VECTORIAL PARALLEL FINITE-ELEMENT CONTRAST SOURCE INVERSION METHOD

Amer Zakaria*, **Ian Jeffrey, and Joe LoVetri**

Department of Electrical and Computer Engineering, University of Manitoba, Winnipeg, MB R3T 5V6, Canada

Abstract—The multiplicatively regularized finite-element contrast source inversion algorithm (MR-FEM-CSI) is used to solve the full-vectorial three-dimensional (3D) inverse scattering problem. The contrast and contrast-source optimization variables are located at the centroids of tetrahedra within the problem domain; whereas the electric field is expanded in terms of edge basis functions on the same tetrahedra. A dual-mesh is created in order to apply the multiplicative regularization. To handle large-scale problems the inversion algorithm is parallelized using the MPI library, with sparse matrix and vector computations supported by PETSc. The algorithm is tested using experimental datasets obtained from the Institut Fresnel database. A synthetic example shows that the technique is able to successfully image moisture hot-spots within a partially filled grain bin.

1. INTRODUCTION

Microwave imaging (MWI) is a modality that quantitatively reconstructs the electrical properties (i.e., the complex permittivity and/or conductivity) of an object-of-interest (OI), thereby also providing an estimate of the OI's shape and location. Optimization algorithms attempt to solve the associated inverse scattering problem by choosing the electrical properties that minimize a cost functional that incorporates the measured microwave field data and a model of the physics. Regularization methods are required to deal with the inherent ill-posedness of the problem. Common regularization methods introduce either additive or multiplicative terms to the functional.

While the majority of MWI algorithms solve two-dimensional (2D) problems, considerable effort has been applied to developing

Received 7 August 2013, Accepted 7 September 2013, Scheduled 11 September 2013
* Corresponding author: Amer Zakaria (zakaria@cc.umanitoba.ca).

algorithms for three-dimensional (3D) applications. Recent work for 3D problems include: multiplicatively regularized (MR) Gauss-Newton inversion (GNI) by Abubakar et al. [1], GNI combined with a discrete dipole approximation (DDA) by Grzegorczyk et al. [2], holographic 3D MWI by Amineh et al. [3] and imaging using a hybrid iterative inversion method that combines contrast source inversion (CSI) and the conjugate-gradient method (CGM) by Mudry et al. [4]. The fastest of the 3D algorithms, for breast cancer imaging, currently seems to be GNI combined with the DDA where high efficiency is obtained through specific assumptions made of the lossy background medium. The state-of-the-art in 3D holographic imaging is limited to qualitative reconstruction of the object-of-interest (OI) [3]. The MR-GNI algorithm and the hybrid CSI-CGM algorithm require a Green's function as they solve integral-equation formulations of the MWI problem; determining the Green's function for complicated imaging chamber boundaries and/or inhomogeneous backgrounds can be complicated and computationally expensive [5]. This requirement is circumvented by introducing sufficient loss into the background medium such that the chamber walls are not "seen". Of course this limits the achievable dynamic range in the measurements which is counter-productive in terms of achieving the best resolution. Whether or not such solutions are beneficial to the imaging results is irrelevant when dealing with applications where one does not have the ability to introduce such a lossy medium, as is the case in the grain-bin imaging application considered as an example herein. In these low-loss cases the PEC boundaries of the chamber must be taken into account by the model being used.

In this work we develop a 3D MWI algorithm that is applicable to a wide variety of physical imaging systems: a finite-element (FEM) based CSI algorithm. The CSI algorithm is a state-of-the-art technique that has had much success solving nonlinear ill-posed electromagnetic inverse scattering problems associated with microwave imaging [6]. Traditionally 3D CSI has been based on integral equation formulations of Maxwell's equations on a regular grid [7] and, similar to MR-GNI, requires determining the appropriate Green's function. An FEM discretization of the problem enables arbitrary boundary conditions [8], inhomogeneous background media [9] and variable mesh density [10] to be built into the model directly. Recently, these benefits have been shown for the 2D scalar [8, 9] and vector FEM-CSI [11, 12] using synthetically generated as well as experimental data.

In this work, we discuss the development of 3D FEM-CSI. Our implementation currently uses LU-decomposition which, while not memory efficient, removes the need for robust pre-conditioners in

iterative solution schemes. Parallelization of the algorithm using PETSc provides a means for handling large problems and a mechanism for a seamless transition to iterative schemes in the future [13]. Our focus is the flexibility that comes with the use of FEM discretization of the MWI problem. FEM-CSI is an invaluable tool for testing and/or improving the design of MWI apparatus and for extending the range of MWI applications; the latter is demonstrated by means of a novel imaging application in the numerical results.

The paper is organized as follows: the mathematical problem and its discretization using FEM are outlined in Section 2; the description of the inversion algorithm, including a novel 3D dual-mesh implementation of a multiplicative regularizer (MR), is given in Section 3; the inversion results using synthetic and experimental datasets are shown and discussed in Section 4; and the paper is concluded in Section 5.

2. PROBLEM STATEMENT

An object-of-interest (OI), immersed in an inhomogeneous background medium within an imaging domain $\mathcal{D}$, is illuminated successively by T sources of electromagnetic radiation at a single frequency f or at a discrete set of frequencies. The OI and the background medium are both assumed non-magnetic, i.e., $\mu = \mu_0$ the permeability of free-space. The contrast, χ, of the OI is defined as

$$\chi(\vec{r}) \triangleq \frac{\epsilon_r(\vec{r}) - \epsilon_b(\vec{r})}{\epsilon_b(\vec{r})}. \tag{1}$$

Here ϵ_r and ϵ_b are, respectively, the complex permittivities of the OI and background relative to the vacuum permittivity ϵ_0, and $\vec{r} = x\hat{x} + y\hat{y} + z\hat{z}$ is a 3D position vector in the Cartesian coordinates. Outside $\mathcal{D}$, $\chi \equiv 0$.

For a transmitter t, the scattered field $\vec{E}_t^{\text{sct}}$ due to the presence of the OI is governed by the following vector wave equation inside a computational domain $\Omega \supseteq \mathcal{D}$:

$$\nabla \times \nabla \times \vec{E}_t^{\text{sct}}(\vec{r}) - k_b^2(\vec{r})\ \vec{E}_t^{\text{sct}}(\vec{r}) = k_b^2(\vec{r})\ \vec{w}_t(\vec{r}). \tag{2}$$

Here $k_b(\vec{r}) = 2\pi f\sqrt{\mu_0\epsilon_0\epsilon_b(\vec{r})}$ is the background wave-number, and $\vec{w}_t(\vec{r}) \triangleq \chi(\vec{r})\vec{E}_t(\vec{r})$ is the contrast source variable where the total field $\vec{E}_t(\vec{r}) = \vec{E}_t^{\text{inc}}(\vec{r}) + \vec{E}_t^{\text{sct}}(\vec{r})$: the incident field $\vec{E}_t^{\text{inc}}(\vec{r})$ is the field in Ω due to sources that radiate in the presence of ϵ_b when the OI is absent, i.e., $\chi = 0$. The fields in this work are considered time-harmonic with an $\exp(j2\pi f\tau)$ time-dependency, where τ is the time variable and $j^2 = -1$.

For a given set of boundary conditions (BCs), the vectorial partial differential Equation (2) can be solved using FEM with the Rayleigh-Ritz variational method [14]. The problem domain, Ω, is divided into a mesh of N tetrahedral elements defined by a set of nodes interconnected via E edges. Each edge is associated with linear vector basis functions whose parameters are dependent on the geometry of the mesh. The resulting FEM matrix equation is

$$\boldsymbol{\mathcal{H}}_b[\underline{E}_t^{\text{sct}}] = \vec{\boldsymbol{\mathcal{R}}}_b \cdot \underline{\vec{w}}_t. \tag{3}$$

Here, the data vector $\underline{E}_t^{\text{sct}} \in \mathbb{C}^E$ contains the scattered field values along the edges of mesh tetrahedra, and $\underline{\vec{w}}_t \in \mathbb{C}^I$ is a column vector that holds the contrast source spatial-vector fields located at the I centroids inside the imaging domain $\mathcal{D}$. The matrix $\boldsymbol{\mathcal{H}}_b \in \mathbb{C}^{E\times E}$ is the FEM discretization matrix which depends on the BCs and the background medium properties, while $\vec{\boldsymbol{\mathcal{R}}}_b \in \mathbb{C}^{E\times I}$ is a matrix dependent on the background medium properties and accounts for projecting the contrast source variables in $\mathcal{D}$ onto the mesh edges in Ω [11, 15]. Both matrices $\boldsymbol{\mathcal{H}}_b$ and $\vec{\boldsymbol{\mathcal{R}}}_b$ are sparse and are independent of the transmitters and object-of-interest. In the inversion algorithm, they are constructed once, saved and recalled when necessary.

Given the contrast source variables $\underline{\vec{w}}_t$, the scattered field along edges is calculated as

$$\underline{E}_t^{\text{sct}} = \boldsymbol{\mathcal{H}}_b^{-1}[\vec{\boldsymbol{\mathcal{R}}} \cdot \underline{\vec{w}}_t] = \vec{\boldsymbol{\mathcal{L}}}[\underline{\vec{w}}_t] \tag{4}$$

where $\vec{\boldsymbol{\mathcal{L}}} \in \mathbb{C}^{E\times I}$ is the "inverse" FEM operator.

3. INVERSION ALGORITHM

Within the framework of the finite-element method, the discretization of the CSI functional results in the following cost functional over the discrete vectors $\underline{\chi}$ and $\underline{\vec{w}}_t$:

$$\mathcal{F}^{\text{CSI}}(\underline{\chi}, \underline{\vec{w}}_t) = \mathcal{F}^{\mathcal{S}}(\underline{\vec{w}}_t) + \mathcal{F}^{\mathcal{D}}(\underline{\chi}, \underline{\vec{w}}_t). \tag{5}$$

Here the normalized data-error term $\mathcal{F}^{\mathcal{S}}(\underline{\vec{w}}_t)$ and the normalized domain-error term $\mathcal{F}^{\mathcal{D}}(\underline{\chi}, \underline{\vec{w}}_t)$ are given by

$$\begin{aligned}
\mathcal{F}^{\mathcal{S}}(\underline{\vec{w}}_t) &= \frac{\sum_t \left\| \underline{\vec{E}}_t^{\text{sct,meas}} - \vec{\boldsymbol{\mathcal{M}}}_{\mathcal{S},t} \vec{\boldsymbol{\mathcal{L}}}[\underline{\vec{w}}_t] \right\|_{\mathcal{S}}^2}{\sum_t \left\| \underline{\vec{E}}_t^{\text{sct,meas}} \right\|_{\mathcal{S}}^2} \\
\mathcal{F}^{\mathcal{D}}(\underline{\chi}, \underline{\vec{w}}_t) &= \frac{\sum_t \left\| \underline{\chi} \odot \underline{\vec{E}}_t^{\text{inc}} - \underline{\vec{w}}_t + \underline{\chi} \odot \vec{\boldsymbol{\mathcal{M}}}_{\mathcal{D}} \vec{\boldsymbol{\mathcal{L}}}[\underline{\vec{w}}_t] \right\|_{\mathcal{D}}^2}{\sum_t \left\| \underline{\chi} \odot \underline{\vec{E}}_t^{\text{inc}} \right\|_{\mathcal{D}}^2}.
\end{aligned} \tag{6}$$

For a transmitter t, $\underline{\vec{E}}_t^{\text{sct,meas}} \in \mathbb{C}^{R_t}$ is a vector of the measured scattered field at R_t receiver locations per transmitter located on the surface $\mathcal{S}$, $\underline{\chi} \in \mathbb{C}^I$ corresponds to a vector of the contrast values located at the tetrahedra centroids in the domain $\mathcal{D}$, and $\underline{\vec{E}}_t^{\text{inc}} \in \mathbb{C}^I$ holds the incident field vector values at the tetrahedra centroids in $\mathcal{D}$.

The operators $\vec{\boldsymbol{\mathcal{M}}}_{\mathcal{S},t} \in \mathbb{C}^{R_t \times E}$ and $\vec{\boldsymbol{\mathcal{M}}}_{\mathcal{D}} \in \mathbb{C}^{I \times E}$ are interpolatory matrix operators that transform field values calculated along the E mesh edges to spatial-vector field values at either the location of the R_t receivers on $\mathcal{S}$ or at the centroids of the tetrahedra inside the imaging domain $\mathcal{D}$.

At each iteration of the algorithm, two steps are performed successively. First, the contrast source variables, $\underline{\vec{w}}_t$, are updated by a conjugate-gradient (CG) method with Polak-Ribère search directions; here the contrast variables, $\underline{\chi}$, are held constant. The second step involves updating $\underline{\chi}$ analytically by minimizing the domain-error functional; the contrast source variables and the domain-error term normalization factor are assumed constant [16]. Additional details about the formulation of FEM-CSI can be found in [8, 11, 15].

3.1. Multiplicatively Regularized CSI

The weighted L_2-norm total variation multiplicative regularization (MR) can be applied to the algorithm which we then refer to as MR-FEM-CSI. With the MR term, the functional at the nth iteration is written as [17]

$$\mathcal{F}_n(\underline{\chi}, \underline{\vec{w}}_t) = \mathcal{F}_n^{\text{MR}}(\underline{\chi}) \times \mathcal{F}^{\text{CSI}}(\underline{\chi}, \underline{\vec{w}}_t) \tag{7}$$

where the regularization term is given by

$$\mathcal{F}_n^{\text{MR}}(\underline{\chi}) = \frac{1}{V} \int_{\mathcal{D}} \frac{\left|\nabla \underline{\chi}\right|^2 + \delta_n^2}{\left|\nabla \underline{\chi}_{n-1}\right|^2 + \delta_n^2}\, dv. \tag{8}$$

Here V is the total volume of the domain $\mathcal{D}$, and $\delta_n^2 = \mathcal{F}^{\mathcal{D}}(\underline{\chi}_n^{\text{CSI}}, \underline{\vec{w}}_{t,n})\, \bar{A}^{-1}$ is a steering factor in which $\bar{A}$ is the mean area of the facets for tetrahedra in $\mathcal{D}$.

With the introduction of MR into the functional, the update procedure of the contrast variables must be modified. After calculating the contrast variables in CSI, they are updated by a CG method using Polak-Ribère search directions. The calculation of the search directions now requires the evaluation of the spatial gradient and divergence of the contrast, which is not straightforward due to the distribution of the unknowns on an unstructured mesh. For this purpose, a 3D dual-mesh technique analogous to the 2D scheme presented in [18] is used.

In this scheme, the spatial gradient is approximated at the nodes of elements inside the imaging domain $\mathcal{D}$, whereas the divergence calculation is performed at the centroids of each tetrahedron inside the imaging domain.

First, a volume Ω_i is constructed surrounding a node i that belongs to domain $\mathcal{D}$. The boundary, Γ_i, of the region Ω_i is built from triangular patches whose vertices are the centroids of tetrahedra sharing the node as shown in Fig. 1. Letting ζ stand for one of the Cartesian coordinates (i.e., x, y, or z), for node i we can approximate the spatial gradient as

$$\frac{\partial \chi_{i,n}}{\partial \zeta} = \hat{\zeta} \cdot \nabla \chi_{i,n} \approx \left\langle \hat{\zeta} \cdot \nabla \chi_n(\vec{r}) \right\rangle_{\Omega_i} = \frac{1}{V_i} \oint_{\Gamma_i} \chi_n(\vec{r}) \hat{\zeta} \cdot \hat{n} \, ds \tag{9}$$

where $\hat{\zeta}$ is a constant unit vector, $\langle \cdot \rangle_{\Omega_i}$ the average value over the volumetric region Ω_i, V_i the volume of Ω_i, and $\hat{n}$ the outward normal vector to Γ_i. The equality in (9) holds as node i is the barycenter of region Ω_i. As $\chi_n(\vec{r})$ is known at the vertices of surface Γ_i, the integration can be performed numerically.

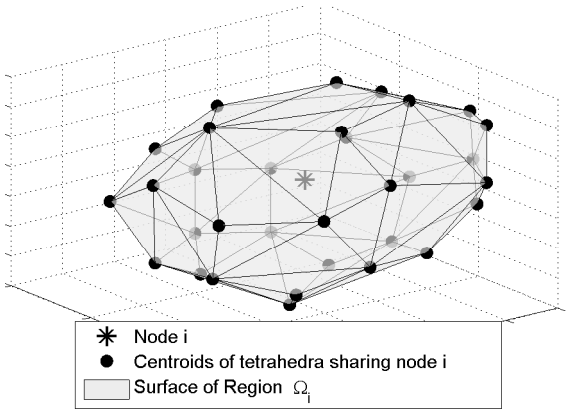

Figure 1. Region surrounding a node i used for evaluating the spatial gradient of the contrast function. Only the dual-mesh is shown.

For calculating the divergence at tetrahedra centroids, scalar first-order linear basis functions are used. For a tetrahedral element e, a vector $\vec{\xi}^e$ can be written as

$$\vec{\xi}^e = \sum_{l=1}^{4} \left(\xi^e_{x,l} \hat{x} + \xi^e_{y,l} \hat{y} + \xi^e_{z,l} \hat{z} \right) \alpha^e_l(\vec{r}) \tag{10}$$

where for a node l (one of the four vertices making up element e) the 3D scalar linear basis function $\alpha_l^e(\vec{r})$ is given as

$$\alpha_l^e(\vec{r}) = \frac{1}{6V^e}\left(a_l^e + b_l^e x + c_l^e y + d_l^e z\right). \tag{11}$$

Here V^e is the volume of element e, and the coefficients a_l^e, b_l^e, c_l^e and d_l^e are only dependent on the tetrahedron geometry [14]. The spatial divergence within a tetrahedron e is then calculated as

$$\nabla\cdot\vec{\xi}^e = \frac{\partial\xi^e}{\partial x}\cdot\hat{x} + \frac{\partial\xi^e}{\partial y}\cdot\hat{y} + \frac{\partial\xi^e}{\partial z}\cdot\hat{z} = \frac{1}{6V^e}\sum_{l=1}^{3}\left(\xi_{x,l}^e b_l^e + \xi_{y,l}^e c_l^e + \xi_{z,l}^e d_l^e\right). \tag{12}$$

Using the nodal values of $\xi_{x,l}^e$, $\xi_{y,l}^e$ and $\xi_{z,l}^e$ calculated by the approximation in (9), the divergence values at the centroids of tetrahedral elements in $\mathcal{D}$ are computed and used to calculate the search directions. More details on including MR in CSI can be found in [19].

4. ALGORITHM IMPLEMENTATION

The fully-vectorial MR-FEM-CSI algorithm has been implemented in C/C++ for distributed memory systems using MPI under the PETSc framework [13]. At the core of this algorithm is the "inverse" of the FEM operator, $\vec{\boldsymbol{\mathcal{L}}}$, a rectangular matrix that maps contrast sources, located at tetrahedra centroids, to scalar tangential fields along the unique tetrahedra edges in the computational domain Ω. Note that the MR-FEM-CSI inversion algorithm operates on the imaging domain $\mathcal{D} \subseteq \Omega$. A flexible parallel implementation should attempt to provide linear scaling of operations performed on both domains, $\mathcal{D}$ and Ω, as the number of processors P increases. For the following reasons, PETSc has been adopted to facilitate the parallel implementation [13, 20]. PETSc is a collection of data-structures and computational routines designed for parallel solutions of sparse systems of equations arising from partial differential equations. In the MR-FEM-CSI formulation, PETSc is well-suited to handle the sparsity of the operators $\boldsymbol{\mathcal{H}}_b$, $\vec{\boldsymbol{\mathcal{R}}}_b$, $\vec{\boldsymbol{\mathcal{M}}}_{\mathcal{S},t}$ and $\vec{\boldsymbol{\mathcal{M}}}_{\mathcal{D}}$. While the focus of this work is limited to producing the operator $\vec{\boldsymbol{\mathcal{L}}}[\underline{\vec{w}}_t]$ explicitly by means of an LU-decomposition, PETSc offers additional features that we will seek to exploit in future work: an array of preconditioners and iterative solvers as well as a GPU interface. Herein, the LU-decomposition of the FEM operator was performed by enabling the SuperLU_Dist library in PETSc [21].

A major benefit of PETSc is that parallel storage and operations can be transparent to the implementation: once vectors such as $\underline{\chi}$ and operators such as $\boldsymbol{\mathcal{H}}_b$ are filled, PETSc will automatically handle partitioning the workload amongst processors; it remains simply to handle the computation of vector and/or operator elements in an efficient manner. To this end, a rough partition of the global element edges (degrees of freedom in the FEM operator) is determined by applying a partitioning technique, such as orthogonal recursive bisection or hypergraph partitioning, to the volumetric elements using the Zoltan library [22]. This assigns an equal partition of geometrically localized elements to each processor. A unique global indexing scheme is then applied to element edges. Processors then compute FEM matrix elements associated with the edges of elements that are locally assigned.

For efficient scalability, the fundamental operations of the algorithm need to be parallelized. On the other hand, we do not attempt to parallelize the algorithm over transmitters due to the limited speed-up that this can achieve in many-processor systems. As the bulk of the memory used in the MR-FEM-CSI algorithm is required for storing the LU-decomposition of the FEM operator, memory limits are not bound by the size of the FEM mesh itself thus the mesh can be duplicated in its entirety on each processor. Nevertheless, if one wished to use a fully distributed mesh representation, additional "ghost" elements are required when applying MR for evaluating the surface integral in (9). In our implementation, the mesh is distributed amongst the processors.

5. INVERSION RESULTS

The results presented in this section were computed using a cluster of 32 8-core Intel Xeon X5355 processors connected by a DDR InfiniBand interconnect. Each of the 256 cores operates at 2.6 GHz and each 8-core processor has 16 GB of memory, or 2 GB per core in a many-core configuration.

The geometry files and meshes used herein were created and optimized using GMSH [23].

In Table 1, the following information is provided for each example: the frequencies (f), the number of transmitters per frequency (T), the number of tetrahedra (N) and edges (E) in the problem domain Ω, the number of unknowns (I) inside the imaging domain $\mathcal{D}$, the average time per iteration (t_{iter}) in seconds (s), the number of processor cores used, the algorithm overhead time, and the memory allocated by each core in megabytes (MB). The algorithm's computational overhead is the time

Table 1. Summary of inversion examples.

Example	f (GHz)	T	N	E	I	t_{iter} (s)
Synthetic Dataset	0.07	24	148,994	179,795	80,047	30
Fresnel Datasets		36				
Two Spheres	3–5		330,274	395,019	173,713	87
Two Cubes	3–8		349,653	416,892	83,020	85
Myster	3–8		302,630	361,980	70,908	81

Example	Number of Processor Cores	Overhead Time (s)	Memory per Core mem/core (MB)
Synthetic Dataset	32	150	309
Fresnel Datasets	96		
Two Spheres		530	411
Two Cubes		530	520
Myster		540	460

required by the code to read in the mesh, create the transformation matrices, allocate memory for vectors, calculate the CSI initial guess and to perform the LU-decomposition of $\boldsymbol{\mathcal{H}}_b$. The latter presents the bulk of the overhead. Storing the LU-decomposition of $\boldsymbol{\mathcal{H}}_b$ is, by far, the greatest contributor to memory use.

In running the MR-FEM-CSI algorithm, at the end of each iteration the estimates of the algorithm were constrained to lie within physical bounds such that $\text{Re}(\epsilon_r) \geq 1$ and $\text{Im}(\epsilon_r) \leq 0$.

5.1. Synthetic Data

The synthetic example investigates the feasibility of detecting spoilage in grain bins using microwave imaging. This MWI application is of current interest and the use of FEM eases the modeling of the problem: the chamber walls are metallic and are modeled as perfect electrically conductive (PEC) boundaries; the background medium is inhomogeneous consisting of a dry-wheat layer and free-space. With FEM it is not necessary to compute a Green's function that accounts for both the PEC and the inhomogeneous background, making FEM-CSI an ideal candidate for solving this problem.

A hopper-style bin, depicted in Fig. 2, whose dimensions mimic

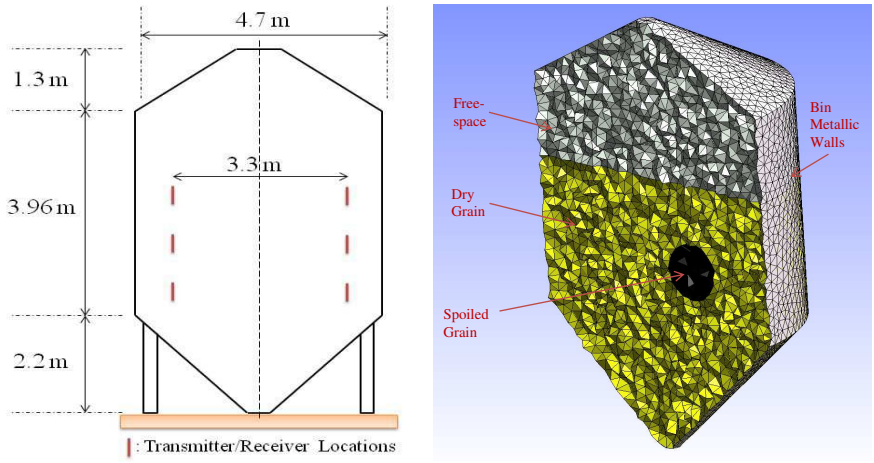

Figure 2. (a) The 2D configuration of the hopper-style bin with transducers' location. (b) A cross-sectional image of the 3D mesh of the bin including a region of spoilage.

that of a grain bin at the Canadian Wheat Board Centre for Stored Grain research at the University of Manitoba, is modeled; the model consists of the bin with metallic walls filled two-thirds to capacity with dry grain (approximately 4.7 m from the based of the bin). Dry grain is loss-less with a dielectric constant of 2 at 70 MHz [24]. Within the grain, a spherical spoilage region of 50 cm diameter is embedded. The center of the spoilage is located at $(0,\ 75,\ -99)$ cm. The relative permittivity of the anomaly was set to $\epsilon_r = 4 - j1$ [25]. The content of the bin are illuminated successively by several sources of electromagnetic radiation at a frequency of 70 MHz. The transmitters are located at the three z-planes $z = \{0, -0.875, -1.75\}$ m. At each layer, 8 transmitters are evenly distributed on a circle of radius 1.65 m. The sources are modeled as electric dipoles polarized along the z-axis and are collocated with the receivers. At the receiver locations, two datasets were collected: the first consisted of only the z-component of the electric field, whereas the second measured all three Cartesian components.

Different meshes are used for the purposes of calculating the synthetic data and performing inversions. Further, 10% noise was added as per the method in [1].

The number of tetrahedra and edges in the FEM mesh is 148,994 and 179,795 respectively. The imaging domain was selected to be

a circular cylinder of height 3.75 m and radius 2 m centered around the origin. The number of tetrahedra centroids where optimization unknowns are located inside $\mathcal{D}$ is 80,047. The inversion algorithm was run on 32 cores requiring 309 megabytes (MB) per core, most of which is required to store the LU-decomposition. The time required to perform overhead calculations was approximately 150 seconds. The time per iteration was ≈ 30 seconds. The algorithm converged in 300 iterations.

The reconstruction results using only the z-component of the electric fields are shown in Figs. 3(a), (b); the results using all three field components are given in Figs. 3(c), (d). For both datasets, the location of the hot-spot within the inhomogeneous background (being dry-wheat and air) was successfully detected. Using all three field components, the spherical construction of the spoilage was better estimated, which is expected as more information is available for the inversion algorithm (1,728 measurements versus 576 in the single

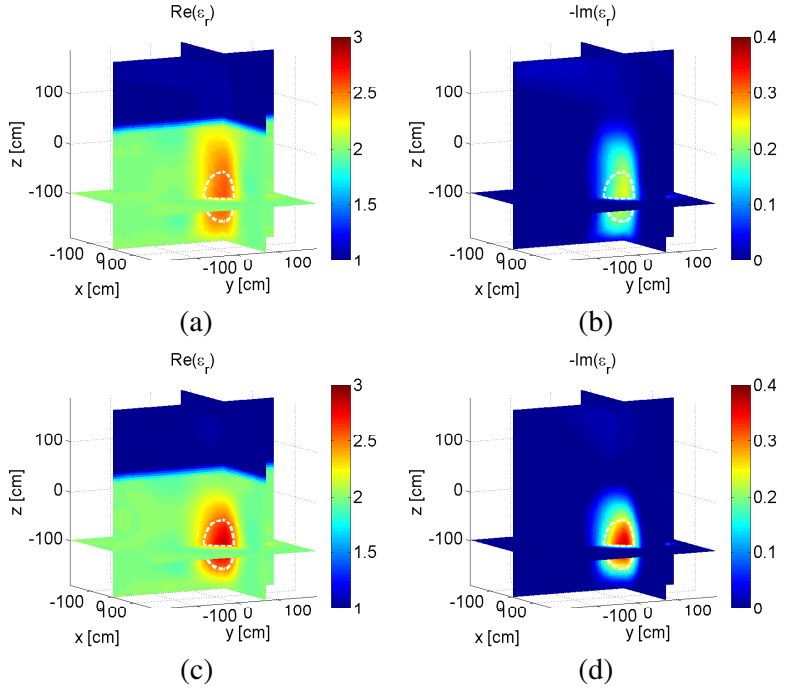

Figure 3. Synthetic dataset reconstruction results collecting (a), (b) only the z-component of the field at the receivers and (c), (d) all field components at the receivers. The white circles show the expected location of the 50 cm spoilage region.

component case). The real and imaginary values of the relative permittivity were underestimated, but are clearly distinguishable from the inhomogeneous background.

The purpose of this synthetic example is to show the ease of using inhomogeneous background along with metallic enclosures in the MR-FEM-CSI algorithm for solving a practical application-of-interest. In this application it is not possible to introduce loss into the background medium, which might then allow the use of a homogeneous infinite-space Green's function.

5.1.1. Parallel Performance

Figure 4 shows the parallel performance of the MR-FEM-CSI code in terms of computational time per iteration and memory requirements per core for parallel runs of the synthetic dataset ranging from 1 to 96 cores. In the serial case, the algorithm required 5.9 GB of memory and 210 seconds/iteration for the 179, 795 mesh edges and 80, 047 imaging domain elements. Parallel scaling exhibits good performance up to 32 cores, where 309 MB of memory are required per core for a total of 9.65 GB of memory. In this configuration the computational time per iteration was 30 seconds, or a speed up of a factor of 7 versus the serial case. Using 32 cores, the number of edges and imaging domain elements associated with each core are approximately 5, 626 and 2, 500 respectively. At this level, communication time and additional parallel overhead related to the LU factorization contribute to the reduction in performance. Beyond 32 cores, the performance continues to increase but with diminishing return. Larger problem sizes, such as those presented for the experimental datasets in the next section, exhibit better parallel performance up to 96 cores.

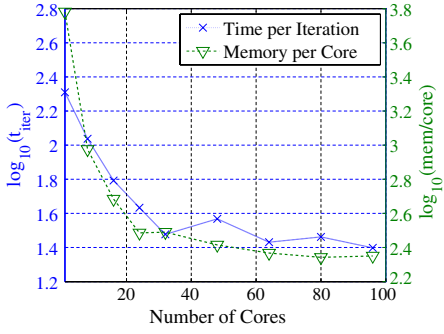

Figure 4. Number of cores vs. $\log_{10}$ (time per iteration/memory per core).

5.2. Fresnel Dataset

Three-dimensional data were collected for several targets at the Institute Fresnel of Marseille in 2009 [26]. The collected datasets have been previously inverted using different methods like MR-IECSI [27], MR-GNI [1], and DBIM [28]. The inversion algorithms were based on the integral-equation formulation of the electromagnetic problem. Herein, the datasets are inverted using the 3D MR-FEM-CSI algorithm.

The experimental setup consisted of a parabolic antenna as a transmitter and a ridge-horn antenna as a receiver, both located inside an anechoic chamber. The antennas moved around the targets on a spherical surface of radius $\approx$ 1.8 m. For the transmitting antenna, the azimuthal angle, ϕ, varied from 20° to 340° with steps of 40° and the polar angle, θ, ranged from 30° to 150° with steps of 15°. The coordinate system definitions used here are shown in Fig. 5. According to the system design, the receiving antenna positions were restricted to a single azimuthal plane at $\theta = 90°$. In addition, for technical reasons the location of the receiving antenna could not be closer than 50° from the azimuth angle position of the transmitter. Hence, the azimuthal angle of the receiver varied from 0° to 350° with steps of 10°, with the exclusion of $\pm 50°$ of the transmitter's azimuthal angle. Furthermore, for each dataset the receiver positions opposite to the transmitter were unusable due to the saturation of the network analyzer.

The measured data were collected at 21 frequencies ranging from 3 GHz to 8 GHz with steps of 0.25 GHz. For each target, the fields were measured at receiver locations for two transmitting antenna

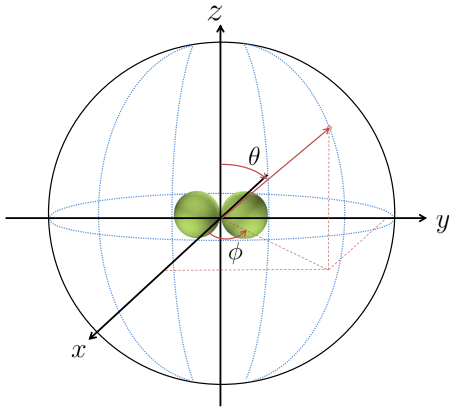

Figure 5. The coordinates configuration of the Institut Fresnel 3D setup.

polarizations: first along θ, then along ϕ. For both cases, the receiver antenna was polarized along the θ-direction. The collected data at each polarization were calibrated using the techniques described in [26].

In this paper the transmitting polarizations were converted to received polarizations by applying reciprocity. Then, as the receiver antenna is always at the $\theta = 90°$ plane, the incident field can be modeled as a z-polarized plane wave with magnitude 1 and phase 0 at the origin (0, 0, 0). The modeled incident field is calculated as

$$\vec{E}_t^{\text{inc}}(\vec{r}) = -e^{jk_b(x\cos(\phi_t')+y\sin(\phi_t'))}\hat{z}. \tag{13}$$

where ϕ_t' denotes the azimuthal angle of the reciprocal transmitter, which is equal to a receiver's azimuthal angle ϕ_r in the actual measurement setup. The plane wave model of the incident field is valid as the transmitters and receivers in the experimental setup are more than 10 wavelengths away from the target.

The receiver locations in the reciprocal system are taken to be at the source positions in the actual measurement setup. The receiver position (ϕ_r', θ_r') corresponds to the transmitter location (ϕ_t, θ_t) in the actual system.

Let $E_{\theta\theta}^{\text{sct}}$ and $E_{\phi\theta}^{\text{sct}}$ be the measured scattered fields at the actual receiver location with the transmitter polarized along the θ- and the ϕ-directions respectively. The spatial components of the scattered field vector at the reciprocal receiver location (ϕ_r', θ_r') are

$$\begin{aligned} E_x^{\text{sct}} &= \cos(\theta_r')\cos(\phi_r')E_{\theta\theta}^{\text{sct}} - \sin(\phi_r')E_{\phi\theta}^{\text{sct}} \\ E_y^{\text{sct}} &= \cos(\theta_r')\sin(\phi_r')E_{\theta\theta}^{\text{sct}} + \cos(\phi_r')E_{\phi\theta}^{\text{sct}} \\ E_z^{\text{sct}} &= -\sin(\theta_r')E_{\theta\theta}^{\text{sct}}. \end{aligned} \tag{14}$$

The multi-frequency reciprocal datasets are inverted using a frequency-hopping approach. That is, data from each frequency are

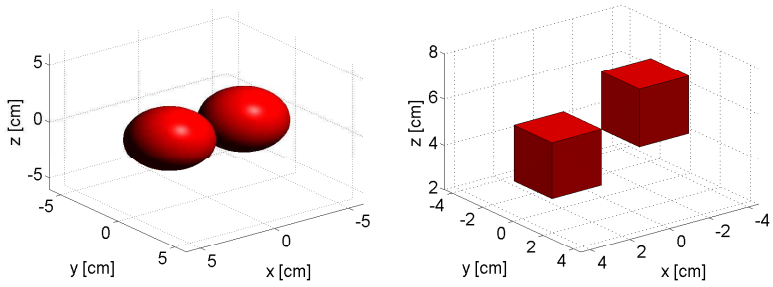

Figure 6. Targets of (a) *Two Spheres* dataset and (b) *Two Cubes* dataset.

inverted independently, and the solution from a lower frequency is used to calculate the initial guess for the next higher frequency. At each frequency, the algorithm was run for 75 iterations (increasing the number of iterations did not alter the final result). Herein we show inversion results for three datasets: *Two Spheres*, *Two Cubes* and *Myster*. The imaginary part of the reconstructions are not shown as the targets are lossless.

5.2.1. Two Spheres

The target consists of two dielectric spheres 50 mm in diameter and aligned along the x-axis, as depicted in Fig. 6(a). The relative permittivity of both spheres is $\epsilon_r = 2.6$. The imaging domain, $\mathcal{D}$, is defined as a sphere 120 mm in diameter, centered around the origin. The unknown variables are located at the centroids of approximately 173,713 tetrahedra within $\mathcal{D}$. The frequency-hopping approach is applied to the multi-frequency data at 3, 4 and 5 GHz.

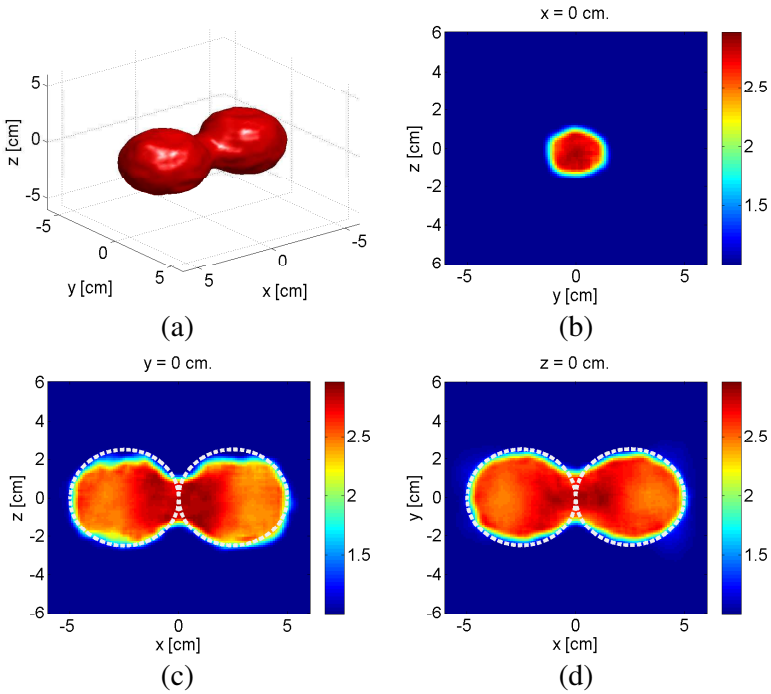

Figure 7. *Two Spheres* reconstruction at 5 GHz: (a) the isosurface plot (level = 1.5), and the 2D cross-section plots at planes (b) $x = 0$, (c) $y = 0$ and (d) $z = 0$. Superimposed circles are provided to show actual OI location.

The results at 5 GHz are shown in Fig. 7 in the form of a 3D isosurface plot (level set to 1.5), and three 2D cross-sectional plots at planes $x = 0$, $y = 0$ and $z = 0$. The algorithm predicated the location and size of the spheres accurately, along with estimating their relative permittivity at approximately 2.6.

5.2.2. Two Cubes

The target/OI has two dielectric cubes of side-length equal to 25 mm and relative permittivity $\epsilon_r = 2.3$. The cubes are located 25 mm and 50 mm above the plane $z = 0$ as shown in Fig. 6(b). The imaging domain, $\mathcal{D}$, is selected as a rectangular prism with length and width equal to 90 mm and a height of 95 mm. The domain center is located at (0, 0, 52.5) mm. The multi-frequency data from 3 GHz to 8 GHz with a step of 1 GHz are used to reconstruct the OI using frequency-hopping approach. The number of unknowns in $\mathcal{D}$ is 83, 020.

The inversion results at 8 GHz are shown in Fig. 8 and they include: (a) an isosurface plot with the level set to 1.5, and the 2D

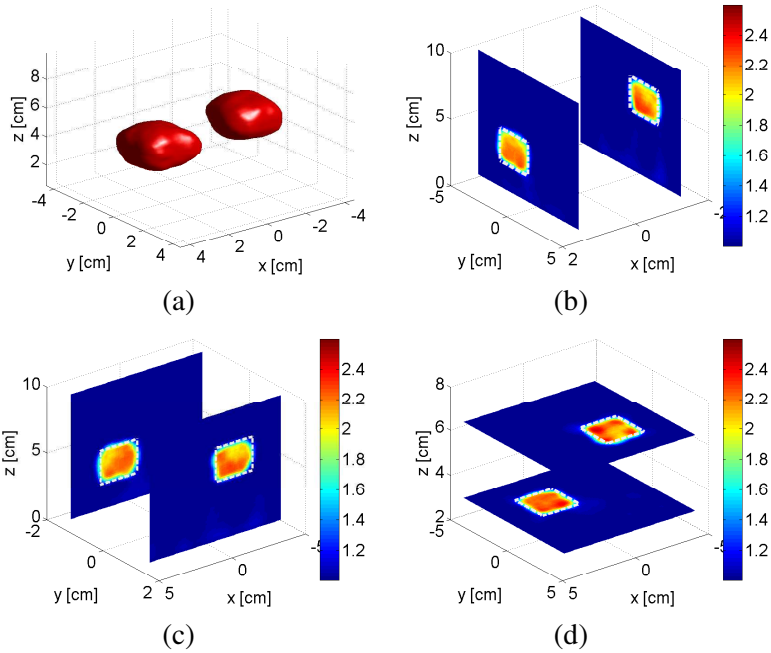

Figure 8. *Two Cubes* reconstruction at 8 GHz: (a) the isosurface plot (level = 1.5), and the 2D cross-section plots at planes (b) $x = [-1.4, 1.4]$ cm, (c) $y = [-1.4, 1.4]$ cm and (d) $z = [3.0, 6.4]$ cm. Superimposed lines are provided to show actual OI location.

slice plots at planes (b) $x = [-1.4, 1.4]$ cm, (c) $y = [-1.4, 1.4]$ cm and (d) $z = [3.0, 6.4]$ cm. The locations and relative sizes of the cubes are predicted correctly by the MR-FEM-CSI algorithm. The estimated relative permittivity values are close to 2.3.

5.2.3. Myster

The target/OI is a group of 12 identical spheres, 23.8 mm diameter each. They are arranged together to compose the geometry shown in Fig. 9(a). The sphere centers are situated along the vertices of an *icosahedron*, as depicted in Fig. 9(b). Each sphere has a relative permittivity $\epsilon_r = 2.6$. The inversion domain, $\mathcal{D}$, is a square box with its center point located at (0, 0, 10) mm. The length and width of the box are equal to 100 mm and its height is 80 mm. The number of unknowns is approximately 70,908. The frequency-hopping approach is applied using data from 3 GHz to 8 GHz with a a frequency increment of 1 GHz.

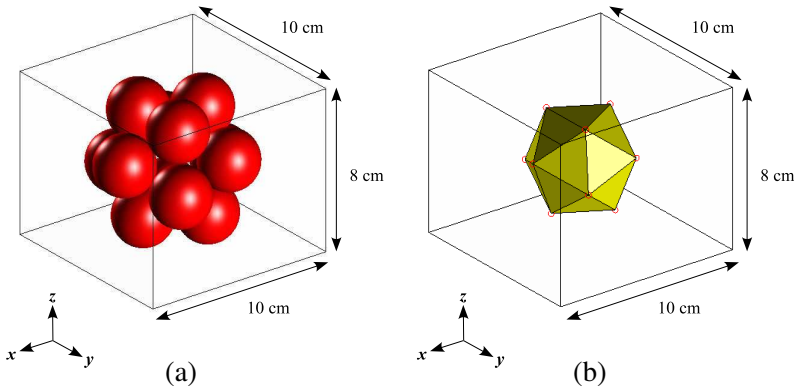

Figure 9. (a) *Myster* target configuration for (b) an icosahedron. The red circles at the vertices of the icosahedron are the centers of spheres constructing the target.

The reconstruction results at 8 GHz are shown in Figs. 10(a)–(f) at six z-planes ranging from $z = 0.44$ cm to $z = 3.567$ cm. The algorithm predicted the overall shape and location of the *Myster* object accurately. The individual spheres of the target are hardly distinguishable from each other and this is due to the nature of the L_2-weighted regularizer that tends to smooth and fuse the spheres together; nevertheless the relative permittivity value of the spheres are not overestimated. These results are similar in accuracy and

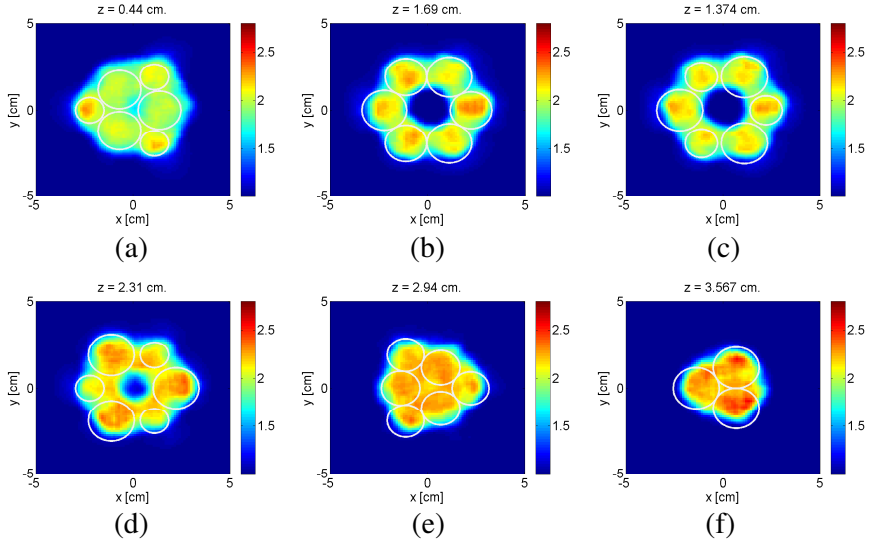

Figure 10. *Myster* reconstruction at 8 GHz: the 2D cross-section plots at z-planes. (a) 0.44 cm, (b) 1.374 cm, (c) 1.69 cm, (d) 2.31 cm, (e) 2.94 cm and (f) 3.567 cm. Superimposed circles are provided to show actual OI location.

performance as those obtained using [1, 27, 28]. MR-FEM-CSI does not provide any significant advantages for the inversion of this type of experimental dataset. But it is interesting to verify the code does compare well with these existing techniques.

6. CONCLUSION

In this work we have presented the extension of the MR-FEM-CSI algorithm to three-dimensional full-vectorial microwave imaging problems. Numerical results have shown successful inversion of both synthetic and experimental datasets. The synthetic dataset was chosen to emphasize the advantages of the FEM formulation, namely boundary conditions of arbitrary type and shape, and support for inhomogeneous background media. In our current implementation, the price for these advantages is the pre-computation and storage of the inverse FEM operator. To reduce the computational burden imposed by storing the LU-decomposition of the FEM operator, we have parallelized the implementation using PETSc.

Future work will consider extending the FEM formulation to higher-order elements, exploiting a dual mesh for supporting the

contrast function and replacing the LU-decomposition of the inverse FEM operator with preconditioned iterative solvers.

ACKNOWLEDGMENT

This work was supported by Natural Sciences and Engineering Research Council of Canada and MITACS Elevate. The authors would like to thank the Institut Fresnel of Marseilles, France, for providing the experimental datasets. Also, the authors acknowledge the help of Mr. Jonatan Aronsson for his assistance in using the cluster at the department of electrical and computer engineering at the University of Manitoba.

REFERENCES

1. Abubakar, A., T. Habashy, G. Pan, and M. Li, "Application of the multiplicative regularized Gauss-Newton algorithm for three-dimensional microwave imaging," *IEEE Tran. on Antenn. and Propag.*, Vol. 60, No. 5, 2431–2441, May 2012.
2. Grzegorczyk, T., P. Meaney, P. Kaufman, R. di Florio-Alexander, and K. Paulsen, "Fast 3-D tomographic microwave imaging for breast cancer detection," *IEEE Tran. on Med. Imaging*, Vol. 31, No. 8, 1584–1592, 2012.
3. Amineh, R. K., A. Khalatpour, and N. Nikolova, "Three-dimensional microwave holographic imaging using co- and cross-polarized data," *IEEE Tran. on Antenn. and Propag.*, Vol. 60, No. 7, 3526–3531, 2012.
4. Mudry, E., P. C. Chaumet, K. Belkebir, and A. Sentenac, "Electromagnetic wave imaging of three-dimensional targets using a hybrid iterative inversion method," *Inverse Probl.*, Vol. 28, No. 6, 065007, 2012, [Online], Available: http://stacks.iop.org/0266-5611/28/i=6/a=065007.
5. Gilmore, C. and J. LoVetri, "Enhancement of microwave tomography through the use of electrically conducting enclosures," *Inverse Probl.*, Vol. 24, No. 3, 035008, 2008, [Online], Available: http://stacks.iop.org/0266-5611/24/i=3/a=035008.
6. Van den Berg, P. M. and R. E. Kleinman, "A contrast source inversion method," *Inverse Probl.*, Vol. 13, No. 6, 1607, 1997.
7. Abubakar, A., P. M. van den Berg, and S. Y. Semenov, "Two- and three-dimensional algorithms for microwave imaging and inverse scattering," *Journal of Electromagnetic Waves and Applications*, Vol. 17, No. 2, 209–231, 2003.

8. Zakaria, A., C. Gilmore, and J. LoVetri, "Finite-element contrast source inversion method for microwave imaging," *Inverse Probl.*, Vol. 26, No. 11, 115010, Nov. 2010, [Online], Available: http://stacks.iop.org/0266-5611/26/i=11/a=115010.
9. Zakaria, A., A. Baran, and J. LoVetri, "Estimation and use of prior information in FEM-CSI for biomedical microwave tomography," *IEEE Antenn. Wirel. Pr.*, Vol. 11, 1606–1609, 2012.
10. Zakaria, A. and J. LoVetri, "A study of adaptive meshing in FEM-CSI for microwave tomography," *The 14th Int. Symp. on Antenna Technology and Applied Electromagnetics & the American Electromagnetics Conf.*, 1–4, Ottawa, Canada, 2010.
11. Zakaria, A. and J. LoVetri, "The finite-element method contrast source inversion algorithm for 2D transverse electric vectorial problems," *IEEE Tran. on Antenn. and Propag.*, Vol. 60, No. 10, 4757–4765, Oct. 2012.
12. Ostadrahimi, M., A. Zakaria, J. LoVetri, and L. Shafai, "A near-field dual polarized (TE-TM) microwave imaging system," *IEEE Tran. on Microw. Theory and Techniques*, Vol. 61, No. 3, 1376–1384, Mar. 2013.
13. Balay, S., J. Brown, K. Buschelman, V. Eijkhout, W. D. Gropp, D. Kaushik, M. G. Knepley, L. C. McInnes, B. F. Smith, and H. Zhang, "PETSc users manual," Argonne National Laboratory, Tech. Rep. ANL-95/11 — Revision 3.3, 2012.
14. Jin, J., *The Finite Element Method in Electromagnetics*, John Wiley and Sons, New York, 2002.
15. Zakaria, A., "The finite-element contrast source inversion method for microwave imaging applications," Ph.D. Dissertation, University of Manitoba, Mar. 2012, [Online], Available: http://hdl.handle.net/1993/5213.
16. Van den Berg, P. M. and A. Abubakar, "Contrast source inversion method: State of art," *Progress In Electromagnetic Research*, Vol. 34, 189–218, 2001.
17. Abubakar, A., T. M. Habashy, and P. M. van den Berg, "Nonlinear inversion of multi-frequency microwave fresnel data using the multiplicative regularized contrast source inversion," *Progress In Electromagnetics Research*, Vol. 62, 193–201, 2006.
18. Zakaria, A. and J. LoVetri, "Application of multiplicative regularization to the finite-element contrast source inversion method," *IEEE Tran. on Antenn. and Propag.*, Vol. 59, No. 9, 3495–3498, Sep. 2011.

19. Van den Berg, P. M., A. Abubakar, and J. Fokkema, "Multiplicative regularization for contrast profile inversion," *Radio Sci.*, Vol. 38, No. 2, 23 (1–10), 2003.
20. Balay, S., J. Brown, K. Buschelman, W. D. Gropp, D. Kaushik, M. G. Knepley, L. C. McInnes, B. F. Smith, and H. Zhang, "PETSc web page," 2012, http://www.mcs.anl.gov/petsc.
21. Li, X. S. and J. W. Demmel, "Super LU DIST: A scalable distributed-memory sparse direct solver for unsymmetric linear systems," *ACM Trans. Mathematical Software*, Vol. 29, No. 2, 110–140, Jun. 2003.
22. Boman, E., K. Devine, L. A. Fisk, R. Heaphy, B. Hendrickson, C. Vaughan, U. Catalyurek, D. Bozdag, W. Mitchell, and J. Teresco, "Zoltan 3.0: Parallel partitioning, load-balancing, and data management services," User's Guide, Sandia National Laboratories, Tech. Report SAND2007-4748W, Albuquerque, NM, 2007.
23. Geuzaine, C. and J.-F. Remacle, "GMSH: A 3-D finite element mesh generator with built-in pre- and post-processing facilities," *International Journal for Numerical Methods in Engineering*, Vol. 79, 1309–1331, 2009.
24. Nelson, S. O., A. W. Kraszewski, S. Trabelsi, and K. C. Lawrence, "Using cereal grain permittivity for sensing moisture content," *IEEE Tran. on Instrum. Meas.*, Vol. 49, No. 3, 470–475, Jun. 2000.
25. Nelson, S. O. and S. Trabelsi, "Dielectric spectroscopy of wheat from 10 MHz to 1.8 GHz," *Meas. Sci. Technol.*, Vol. 17, No. 8, 2294–2298, Jul. 2006.
26. Geffrin, J. M. and P. Sabouroux, "Continuing with the Fresnel database: Experimental setup and improvements in 3D scattering measurements," *Inverse Probl.*, Vol. 25, No. 2, 024001, Feb. 2009.
27. Li, M., A. Abubakar, and P. M. van den Berg, "Application of the multiplicative regularized contrast source inversion method on 3D experimental fresnel data," *Inverse Probl.*, Vol. 25, No. 2, 024006, Feb. 2009, [Online], Available: http://stacks.iop.org/0266-5611/25/i=2/a=024006.
28. Yu, C., M. Yuan, and Q. H. Liu, "Reconstruction of 3D objects from multi-frequency experimental data with a fast DBIM-BCGS method," *Inverse Probl.*, Vol. 25, No. 2, 024007, Feb. 2009, [Online], Available: http://stacks.iop.org/0266-5611/25/i=2/a=024007.